Kasetsart J. (Nat. Sci.) 47 : 460 - 477 (2013)

The k-ε Turbulence Model to Simulate the Two-Phase Flows of Fluids in Flumes using C++ Open Source Code Computational Fluid Dynamic Software

Ekachai Chaichanasiri and Chakrit Suvanjumrat*

ABSTRACT

The governing equations of two-phase flows based on the k-ε turbulence model were developed using open source computational fluid dynamic codes and open field operation and manipulation (OpenFOAM) software to simulate water flows in a flume. The water surface was modeled using the volume of fluid method with a turbulence model. The PISO (pressure implicit with splitting of operator) algorithm was used to solve the pressure-velocity coupling in the two-phase flows. The solutions of the simulations were validated using the experimental results as free surface profiles on the wall of the laboratory flume in transient and steady time periods. The transient time period started from when the water was distributed into the flume until it began to overflow the top of the weirs. The steady time period accounted for the water overflowing the weirs and the surface profiles did not change. It was found that the average error of the surface profiles in the transient and steady time periods obtained from the simulations was 8.94% and 8.06%, respectively.

Keywords: computational fluid dynamics (CFD), turbulence, volume of fluid (VOF) method, flumes, open field operation and manipulation (OpenFOAM)

INTRODUCTION

In fluid mechanics, the flow in a flume is classified as open-channel flow. The flow of a liquid in a flume open to the atmosphere that is characterized by the presence of a liquid-gas interface is called a free surface flow. Where the flow depth changes over a relatively short distance based on a rapidly varied flow, then a non-uniform high surface flow results (Cengel and Cimbala, 2010; Munson *et al.*, 2010). A broad-crested weir is an obstruction in a flume that is used to measure water flow rates. In the flow regime, it induces critical conditions on a crest by raising the flume bed and reducing the specific energy to a minimum. There is then a unique relationship between the flow rate per unit width and the upstream water depth related to the weir crest which is utilized for flow measurements (Henderson, 1966; French, 1987).

Nowadays, studying the surface profile over a flume bed with a broad-crested weir uses turbulence computational fluid dynamic (CFD) models. It is important to design the weir shape to be able to accurately measure the flow and to calculate the appropriate flow structure. Many researchers have used CFD software to simulate the fluid flow over a broad-crested weir in a flume

Department of Mechanical Engineering, Faculty of Engineering, Mahidol University, Nakhon Pathom 73170, Thailand.
* Corresponding author, e-mail: chakrit.suv@mahidol.ac.th

Received date : 08/01/13 Accepted date : 28/03/13

(Sarker and Rhodes, 2004; Hargreaves *et al*., 2007; Yeung, 2007; Haun *et al*., 2011). However, the CFD software packages are mostly commercial software, for which the license fees are too expensive and this restricts further study.

The open field operation and manipulation (OpenFOAM) software is open source software based on the CFD codes. It is written in the C++ language under the GNU general public license, which provides an economical method to develop the turbulence model of two-phase flows (OpenFOAM, 2009). The current study involved the development and implementation of the C++ codes for the k-ε turbulence model based on two-phase flows using the OpenFOAM software to analyze the water surface height changes associated with different flows over the flume bed of a weir. The developed codes can be applied to design the appropriate flow structure and to accurately measure the flow over a weir. In addition, this research will stimulate the use of open source CFD software for application development, which will save the cost of purchasing the commercial software.

MATERIALS AND METHODS

Mathematical model

The basic equation of fluid flow for each continuous phase of two-phase flows in flumes can be obtained by first identifying the appropriate fundamental principles from the conservation of mass and momentum. The phase indicator function $\alpha^k(x,y,z,t)$ was defined to exhibit the fluid phases that were present within the fluid flow by Equation 1:

$$\alpha^k(x,y,z,t)=\begin{cases}1, \ if\,(x,y,z) is\ in\ k^{th}\ phases\ at\ time\ (t)\\ 0, \ otherwise\end{cases} \quad (1)$$

The specific values of α^k were associated with each fluid and disseminated using a volume of fluid (VOF) function as shown in Equation 2:

$$\frac{\partial \alpha^k}{\partial t}+U^f\nabla\alpha^k=0 \quad (2)$$

where U^f is the interface velocity.

The free surface boundary was assigned for the free surface of the flow. The conservation of mass at the interface could be written as Equation 3:

$$\frac{\partial \rho^k\alpha^k}{\partial t}+\alpha^k\nabla\cdot\left(\rho^kU^k\right)=\rho^k\frac{\partial\alpha^k}{\partial t} \quad (3)$$

where $U^f\equiv[u^k, v^k, w^k]$, t is time, ρ^k is the fluid density and u, v and w are the velocity in the x, y and z direction, respectively.

Substituting Equation 2 into Equation 3 and rearranging terms yields Equation 4:

$$\frac{\partial \rho^k\alpha^k}{\partial t}+\nabla\cdot\left(\alpha^k\rho^kU^k\right)=\rho^k\left(U^k-U^f\right)\nabla\alpha^k \quad (4)$$

The $\nabla\alpha^k$ is zero except at the interface for the mass conservation equation in the case of the two-fluid model.

The conservation of momentum at the interface can be determined by multiplying the conservation of momentum by the phase indicator function and employing Equation 4 for a local acceleration term as shown in Equations 5:

$$\frac{\partial \rho^k\alpha^kU^k}{\partial t}+\nabla\cdot\left(\alpha^k\rho^kU^k\otimes U^k\right) \quad (5)$$

$$=-\nabla\left(\alpha^kP^k\right)+\nabla\left(\alpha^k\tau^k\right)+$$

$$+\alpha^k\sum F^k_{external\ forces}+\Omega^k$$

and hence as Equations 6 and 7:

$$U^k\otimes U^k=\begin{Bmatrix}u^k\vec{i}\\ v^k\vec{j}\\ w^k\vec{k}\end{Bmatrix}\left(u^k\vec{i}+v^k\vec{j}+w^k\vec{k}\right) \quad (6)$$

$$\Omega^k=\rho^kU^k\left(U^k-U^f\right)\nabla\alpha^k+P^k_f\nabla\alpha^k+$$

$$\left(P^k-P^k_f\right)\nabla\alpha^k-\tau^k\nabla\alpha^k\simeq F^k \quad (7)$$

where Ω^k is the interfacial momentum source P_f^k, is the interfacial pressure which can occur at any point along the interface and F^k is the total force on the interface (Chaichanasiri and Suvanjumrat, 2012).

Turbulent flow behaves in a random and chaotic manner. In order to reduce the unstable and unsteady behavior to resolve the turbulence water flow, an averaging operator may be applied to the conservation equations of two-phase flow. The classical averaging method is the ensemble average, which produces the Reynolds Average Navier-Stokes equations (RANS). For a time-independent and/or non-cyclic flow, ensemble averaging will produce the same result as time averaging (Versteeg and Malalasekera, 2007; Yeoh and Tu, 2010). The RANS equations for the conservation of mass and momentum are given by Equation 8:

$$\frac{\partial \rho^k \alpha^k}{\partial t} + \nabla \cdot \left(\alpha^k \rho^k U^k \right) = \rho^k \left(U^k - U^f \right) \nabla \alpha^k \quad (8)$$

and hence as Equation 9:

$$\frac{\partial \rho^k \alpha^k U^k}{\partial t} + \nabla \cdot \left(\alpha^k \rho^k U^k \otimes U^k \right) = -\nabla \left(\alpha^k P^k \right)$$

$$+\nabla \left(\alpha^k \left(\left(\mu^k + \mu_T^k \right) \left(\nabla U^k + \left(\nabla U^k \right)^T \right) \right. \right.$$

$$\left. \left. -\frac{2}{3} \left(\mu^k + \mu_T^k \right) \nabla \cdot U^k \delta - \frac{2}{3} \rho^k k^k \delta \right) \right)$$

$$+\alpha^k \sum F_{body\ forces}^k + \alpha^k \sum F_{external\ forces}^k + \Omega^k \quad (9)$$

where μ^k is the viscosity for k^{th} phase. The term μ_T^k is the turbulent viscosity for the k^{th} phase, which can be obtained by Equation 10:

$$\mu_T^k = C_\mu \rho^k \frac{\left(k^k \right)^2}{\varepsilon^k} \quad (10)$$

where k^k is the turbulent kinetic energy and ε^k is the rate of dissipation of turbulent energy.

The values of k^k and ε^k were solved according to their respective transport equations obtained by Equations 11 and 12, respectively.

$$\frac{\partial \rho^k \alpha^k k^k}{\partial t} + \nabla \cdot \left(\alpha^k \rho^k U^k k^k \right) = \nabla \cdot \left(\alpha^k \frac{\mu_T^k}{\sigma^k} \nabla k^k \right) + \alpha^k \left(L^k + G^k + \rho^k \varepsilon^k \right) \quad (11)$$

$$\frac{\partial \rho^k \alpha^k \varepsilon^k}{\partial t} + \nabla \cdot \left(\alpha^k \rho^k U^k \varepsilon^k \right) = \nabla \cdot \left(\alpha^k \frac{\mu_T^k}{\sigma_\varepsilon} \nabla \varepsilon^k \right) + \alpha^k \frac{\varepsilon^k}{k^k} \left(C_{\varepsilon 1} P^k + G^k - C_{\varepsilon 2} \rho^k \varepsilon^k \right) \quad (12)$$

where L^k is the shear production defined by Equation 13 and G^k is the production due to gravity can be written as Equation 14:

$$L^k = \mu_T^k \nabla U^k \cdot \left(\nabla U^k + \left(\nabla U^k \right)^T \right) - \frac{2}{3} \nabla \cdot U^k \left(\rho^k k^k + \mu_T^k \nabla \cdot U^k \right) \quad (13)$$

$$G^k = -\frac{\mu_T^k}{\rho^k \sigma_P^k} g \cdot \nabla \rho^k \quad (14)$$

Launder and Spalding (1974) specified the constants for the k-ε model through comprehensive data fitting for a wide range of turbulence flows at C_μ = 0.09, σ^k = 1.00, σ_ε = 1.3, $C_{\varepsilon 1}$ = 1.44 and $C_{\varepsilon 2}$ = 1.92, respectively.

Finite volume discretization

The intention of the discretized method is to transform the governing equations into the corresponding algebraic equation systems for solving the approximated solutions in space and time domains. This process is facilitated by using the governing equations which can be written in terms of the general transport equation for property

$\varnothing^k$ (Versteeg and Malalasekera, 2007) as shown by Equation 15:

$$\underbrace{\frac{\partial \rho^k \varnothing^k}{\partial t}}_{\textit{Time Derivative}} + \underbrace{\nabla \cdot \rho^k U^k \varnothing^k}_{\textit{Convection Term}} = \underbrace{\nabla \cdot \Gamma^k \nabla \varnothing^k}_{\textit{Diffusion Term}} + \underbrace{S^k}_{\textit{Source Term}} \quad (15)$$

where ρ^k is the density of the k^{th} phase, φ^k is the dependent variable of the k^{th} phase, U^k is the vector of velocity of the k^{th} phase, Γ^k is the diffusion coefficient of the k^{th} phase and S^k is the source term of the k^{th} phase.

The corresponding values of φ^k, Γ^k and S^k for the mass, momentum and k-ε equation of the two-phase flow general transport equations are summarized in Table 1.

An implementation of the finite volume method (FVM) in this study used cells with an arbitrary number of faces as shown in Figure 1. Point *P* is in the center of a cell of interest, which was bounded by flat faces that were shared with the neighboring cells. The vector S_i^f is normal to the flat faces and pointing outward from the cell. The vector $\overline{PN}_i$ connects the computational point *P* with the neighbor points N_i.

The finite volume discretization can be formulated by integrating over the interested control volume ($\forall_P$) and time can be written by Equation 16:

$$\int_t^{t+\Delta t} \left(\int \frac{\partial \rho^k \varnothing^k}{\partial t} d\forall_P + \int \nabla \cdot \left(\rho^k U^k \varnothing^k \right) d\forall_P \right) dt = \int_t^{t+\Delta t} \left(\int \nabla \cdot \left(\rho^k \Gamma^k \nabla \varnothing^k \right) d\forall_P + \int S^k d\forall_P \right) dt \quad (16)$$

The linear variation of $\varnothing^k$ within a time step was used in this study based on the Euler implicit time differencing scheme and is given by Equation 17:

$$\int \frac{\partial \rho^k \varnothing^k}{\partial t} d\forall_P = \frac{\left(\rho^k \varnothing_P^k \right)^{t+\Delta t} - \left(\rho^k \varnothing_P^k \right)^t}{\Delta t} \forall_P \quad (17)$$

where $\varnothing_P^k$ is the general variable of the k^{th} phase at point *P* of the cell of interest and Δt is the time step.

Gauss's theorem can be applied to the convection term for transforming the volume integral to a surface integral as shown in Equation 18:

$$\int \nabla \cdot \left(\rho^k U^k \varnothing^k \right) d\forall_P = \sum_{i=1}^{n} \left(\rho^k U^k \right) \varnothing_f^k S_i^f \quad (18)$$

Table 1 Generic form of the two-phase flow differential equation.

Conservative Equation	ϕ^k	Γ^k	S^k
Mass	α^k	0	0
Momentum	$\alpha^k U^k$	$\alpha^k \mu_{eff}^k$	$-\nabla(\alpha^k P^k) + \alpha^k \sum F_{body\ forces}^k + \alpha^k \sum F_{external\ forces}^k + \Omega^k$
Kinetic energy	k^k	$\alpha^k \frac{\mu_T^k}{\sigma^k}$	$\alpha^k \left(L^k + G^k + \rho^k \varepsilon^k \right)$
Dissipated energy rate	ε^k	$\alpha^k \frac{\mu_T^k}{\sigma_\varepsilon}$	$\alpha^k \frac{\varepsilon^k}{k^k} \left(C_{\varepsilon 1} L^k + G^k - C_{\varepsilon 2} \rho^k \varepsilon^k \right)$

ϕ^k = Dependent variable of the k^{th} phase; ρ^k = Density of the k^{th} phase; U^k = Vector of velocity of the k^{th} phase; Γ^k = Diffusion coefficient of the k^{th} phase; S^k = Source term of the k^{th} phase; $\alpha^k \mu_{eff}^k$ = Effective viscosity for k^{th} phase; Ω^k = Interfacial momentum source; k^k = Turbulent kinetic energy; ε^k = Rate of dissipation of turbulent energy; μ_T^k = Turbulent viscosity for k^{th} phase; L^k = Shear production; G^k = Production due to gravity.

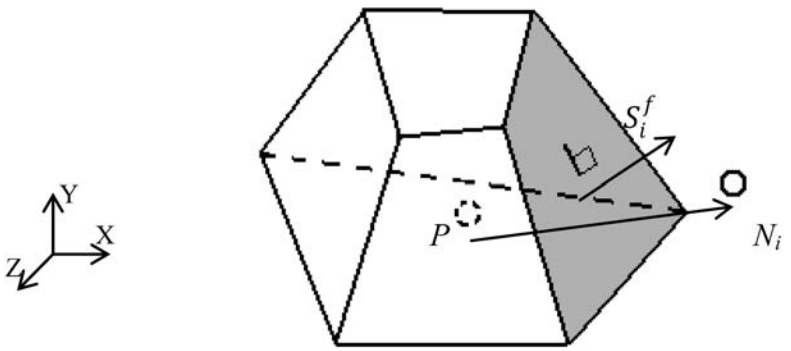

Figure 1 Typical space domain of discretization of the finite volume method. P = the center point of a cell of interest; N_i = the center point of neighboring cells; S_i^f = cell face vector.

where $\varnothing_f^k$ is the general variable of the k^{th} phase on flat faces of the cell of interest and S_i^f is the surface area of the cell of interest.

The Upwind differencing scheme was employed in this study to determine $\varnothing_f^k$ on the face from the direction of flow as written by Equations 19 and 20:

$$\varnothing_f^k = \begin{cases} \varnothing_P^k & for \quad F \geq 0 \\ \varnothing_{N_i}^k & for \quad F < 0 \end{cases} \tag{19}$$

$$\text{when} \quad F = \left(\rho^k U^k\right) S_i^f \tag{20}$$

where F is the convective mass flux through faces of an interested cell.

The diffusion term was integrated over a cell and reduced to Equations 21 and 22:

$$\int \nabla \cdot \left(\rho^k \Gamma^k \nabla \varnothing^k\right) d\forall_P = \sum_{i=1}^{n} \left(\rho^k \Gamma^k\right) \nabla \varnothing_f^k S_i^f \tag{21}$$

when

$$\nabla \varnothing_i^k S_i^f = \frac{\varnothing_{N_i}^k - \varnothing_P^k}{\left|\overline{PN_t}\right|} \left|S_i^f\right| \tag{22}$$

where $\overline{PN_t}$ is any length between the center of the cell of interest and the center of a neighboring cell.

The source terms are defined as Equation 23:

$$\int S^k d\forall_P = S^k \forall_P = \left(S_U^k + S_P^k \varnothing_P^k\right) \forall_P \tag{23}$$

where S_U^k is the explicit source term and S_P^k is the implicit source term.

Using Equations 17, 18, 21 and 23, then Equation 16 can be reformulated as Equation 24:

$$\frac{\left(\rho^k \varnothing_P^k\right)^{t+\Delta t} - \left(\rho^k \varnothing_P^k\right)^t}{\Delta t} \forall_P + \sum_{i=1}^{n} \left(\rho^k U^k\right) \varnothing_f^k S_i^f = \sum_{i=1}^{n} \left(\rho^k \Gamma^k\right) \nabla \varnothing_f^k S_i^f + S_U^k \forall_P + S_P^k \varnothing_P^k \forall_P \tag{24}$$

The discretized equations yield an equation for $\varnothing^k$ in each cell that can be written in terms of neighboring cells as in Equations 25 and 26:

$$a_P^k \left(\varnothing_P^k\right)^{t+\Delta t} = \sum_{i=1}^{n} a_{N_i}^k \left(\varnothing_{N_i}^k\right)^{t+\Delta t} + S_U^k \tag{25}$$

and

$$a_P^k = \sum_{i=1}^{n} a_{N_i}^k - S_P^k \tag{26}$$

where $\varnothing_{N_i}^k$ is the general variable of the k^{th} phase in the neighboring cells, a_P^k is the central coefficient of the k^{th} phase and $a_{N_i}^k$ is the neighboring coefficient of the k^{th} phase.

A problem associated with the calculation of the velocity and pressure on co-located cells can be solved by interpolating the discretized equation onto the cell faces and applying the continuity constraint to the cell face velocities (OpenFOAM, 2009). The discretized equation was modified by extracting pressure as written by Equation 27:

$$a_P^k \left(\varnothing_P^k\right)^{t+\Delta t} = \sum_{i=1}^{n} a_{N_i}^k \left(\varnothing_{N_i}^k\right)^{t+\Delta t} + S_U^k - \nabla P^k \quad (27)$$

The pressure correction was obtained by reformulating Equation 27 to give Equations 28 and 29:

$$\left(U_P^k\right)^{t+\Delta t} = \frac{H\left(U_P^k\right)}{a_P^k} - \frac{1}{a_P^k}\nabla P^k \quad (28)$$

where

$$H\left(U_P^k\right) = \sum_{i=1}^{n} a_{N_i}^k \left(\varnothing_{N_i}^k\right)^{t+\Delta t} + S_U^k \quad (29)$$

For simplicity, the superscript $t + \Delta t$ of Equation 28 can be dropped and the definition of the velocity value at the cell faces was obtained by interpolation of the semi-discretized form of the discretized equation given by Equation 30:

$$U_f^k = \left(\frac{H\left(U^k\right)}{a_P^k}\right)_f - \left(\frac{1}{a_P^k}\nabla P^k\right)_f \quad (30)$$

The discretized form of the continuity equation is obtained from Equation 31:

$$U_f^k = \left(\frac{H\left(U^k\right)}{a_P^k}\right)_f - \left(\frac{1}{a_P^k}\nabla P^k\right)_f \quad (31)$$

Substitution of Equation 30 into Equation 31 gives the following form of the pressure equation obtained by Equation 32:

$$\sum_{i=1}^{n}\left(\frac{\nabla P^k}{a_P^k}\right)_f S_i^f = \sum_{i=1}^{n}\left(\frac{H\left(U^k\right)}{a_P^k}\right)_f S_i^f \quad (32)$$

The terms containing the pressure were now defined in terms of a cell and its nearest neighbors and were formulated by the pressure Equations 33 and 34:

$$a_P^k P_P^k = \sum_{i=1}^{n} a_{N_i}^k P_N^k + S_P^k \quad (33)$$

where

$$S_P^k = \sum_{i=1}^{n}\left(\frac{H\left(U^k\right)}{a_P^k}\right)_f S_i^f \quad (34)$$

The PISO (pressure implicit with splitting of operator) algorithm for solving the couple pressure-velocity in the transient flow calculations developed by Issa (1986) was used in this study. It can be described as:

(a) Momentum Prediction: Equation 28 was solved first using a guessed field of P^{k*} to give a new velocity field (U^{k*}).

(b) Pressure Solution: The $H(U^{k*})$ operators were assembled using the predication of U^{k*}. The pressure solution of Equation 33 gave rise to a new pressure field P^{k**}.

(c) Explicit Velocity Correction: With the new pressure field, the velocity was determined explicitly using Equation 28. The new velocity U^{k**} was now consistent with the new pressure field.

(d) Update of $H(U^k)$ equation: The U^{k**} was used to calculated the $H(U^{k**})$operator for giving rise to P^{k***} which in turn was used to calculate U^{k***}.

The loop of the PISO algorithm consisted of an implicit momentum predictor followed by the series of pressure solutions and explicit velocity corrections. This loop was continued until a pre-defined tolerance was reached.

Development and Implementation

In this study, the C++ codes of utility and solver for the k-ε turbulence model were created in the application. The utility involved data manipulation to create the space domain of

the flumes. Triangular and rectangular shapes of the weir block were studied. Figure 2 shows the space domain characteristics of flumes with a rectangular and a triangular weir. The flumes with a rectangular weir and with a triangular weir were divided by non-uniform cells based on the cell or grid-independent study. The hexagonal cells were used with refinement in the near-weir regions and in the expected regions of the free surface. The numbers of cells totaled 32,649 and 26,626 for the flumes with a rectangular and triangular weir, respectively. The transport properties of fluid that flowed inside the flumes with weirs are shown in Table 2. The no-slip boundary condition was treated at the sidewall of the flume, the bed of the flume and at weir surfaces, which had velocity at boundaries of zero.

The distribution of water in the approach channel was varied by 2.0, 3.0 and 4.0 $m^3.hr^{-1}$, respectively. The six cases were studied and validated by the experiments which are described in Table 3. The category of solver that contained the turbulence equations, the VOF function and the PISO algorithm was described in the previous section. A transient time step of 0.001 s was used for the calculations in this solver.

Validation setting and procedure

The experiment was conducted in a 2,500 × 55 × 175 mm (length by width by depth) flume which had acrylic sidewalls and an aluminum bed. The weir was located 500 mm along the left edge of the acrylic sidewall. Rectangular and triangular weirs were used to study the weir shape effect. Flow was distributed evenly through a horizontal perforated pipe at the inlet. The distribution flow rate of the water was adjusted using a gate valve and measured using a calibrating tank. Three levels of water flow rate (2.0, 3.0 and 4.0 $m^3.hr^{-1}$ were used in this study. The flume setting is shown in Figure 3. The experiments were carried out with conditions according to the CFD study cases. The experiment in each case was conducted over the period from the water entering an empty flume until the depth of water over the flume bed and weirs was unchanged. The sequences of the water flow in a flume with the rectangular and triangular weir were recorded by a CCD camera (Model scA640-70fm; Basler AG; Ahrensburg, Germany which had an image frame size of 659 × 494 pixels and a speed of 60 frames per second.

Table 2 Properties of fluid.

Fluid phase	ρ(kg/m^3)	$\mu\left(\frac{N}{m^2}\cdot s\right)$
Air	1.18	1.825×10^{-5}
Water	997	0.901×10^{-3}

μ = Viscosity of fluid, ρ= Fluid density. Sourced from: Cengel and Cimbala (2010).

Table 3 Computational fluid dynamics (CFD) cases studied.

CFD case	Weir type	Rate of water distribution ($m^3.hr^{-1}$)		
		2.0	3.0	4.0
1	Rectangular	⊙		
2	Rectangular		⊙	
3	Rectangular			⊙
4	Triangular	⊙		
5	Triangular		⊙	
6	Triangular			⊙

The symbol ⊙ indicates the characteristic set in the CFD models.

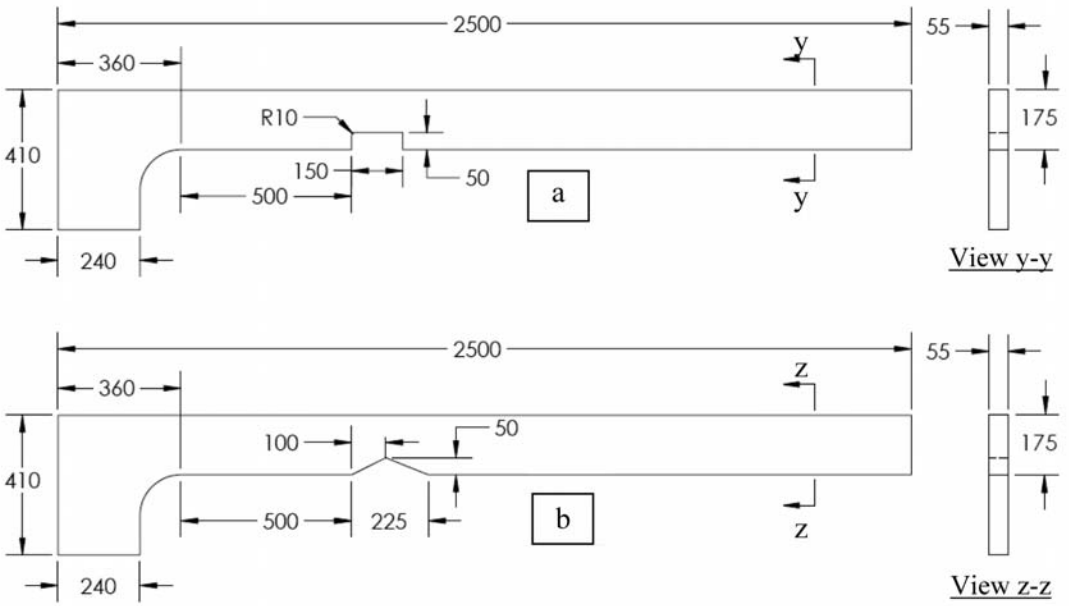

Figure 2 Space domains of the flume with: (a) rectangular weir and (b) triangular weir. All units are in millimeters.

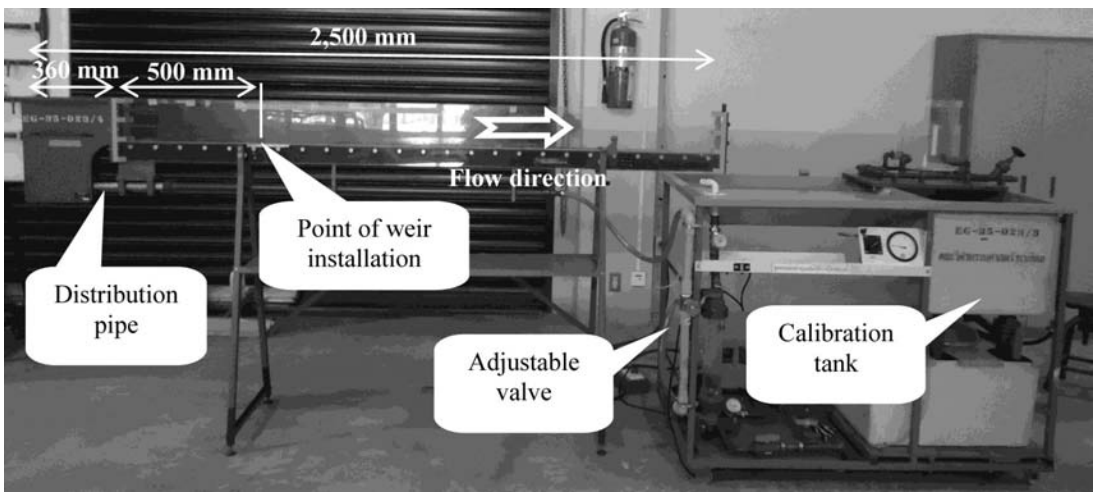

Figure 3 Rectangular flume (length 2,500 mm) and flow-control devices.

RESULTS AND DISCUSSION

Figure 4 shows the sequences of water flow at the rate of 3.0 $m^3.hr^{-1}$ into the experimental flume with a rectangular weir installed. The behavior of the water flow as it crashed onto the front of the weir (the left hand side of a rectangular weir) was like the flow from a dam break. In the transient time (t) period ($t < 5.5$ s), the water surface jumped and moved back in front of the rectangular weir until it flowed over the top of weir. The water surface crest moved in a reverse upstream direction and disappeared at $t = 5.5$ s that marked the commencement of water

overflow at the rectangular weir. Figure 5 shows the sequences of water flow into the experimental flume with a triangular weir using the same time of the flow sequence as in the flume with the rectangular weir. The velocity of the reverse flow was investigated from the backward movement of the surface crest in front of the weirs. The rectangular weir had more severe breaking of the water flow than the triangular weir. This can be observed from Figures 4 and 5, where the crest of the water wave in the case of the rectangular weir travels to the left of the flume faster than with the triangular weir. The inclination of the triangular weir face reduced the severity of water breaking and the velocity of the reverse flow of the water surface crest. The finite volume models were simulated according to the experiments. The simulations were run for 20 s to investigate the many steps of the surface profiles of water flow into the flume. The sequences of the CFD results of a flume with a rectangular or a triangular weir are shown in Figures 6 and 7, respectively, to compare

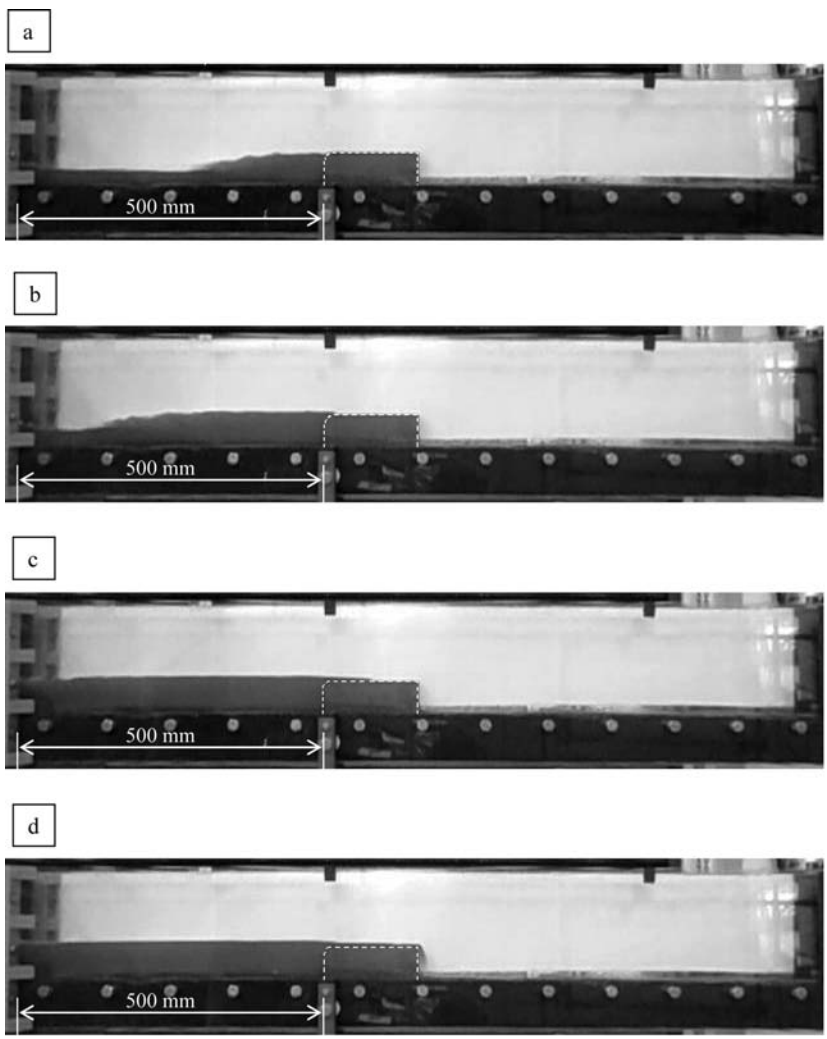

Figure 4 Sequential images of water flowing into a flume with a rectangular weir (outlined with a dotted white line) at a flow rate of 3.0 $m^3.hr^{-1}$ at time: (a) t = 4.0 s; (b) t = 4.5 s; (c) t = 5.0 s; (d) t = 5.5 s.

with the experimental results in Figures 4 and 5, respectively. It was found that the surface profile of the CFD corresponded with the experiment.

The experiment and CFD were performed using three flow rates. The heights of the water surface over the flume bed and weirs in the experiments were detected using the SloshDetector software (Suvanjumrat and Puttapitukporn, 2010). The comparisons between the transient simulation and experiment of surface profiles at various times (t = 4.0, 4.5, 5.0 and 5.5 s) for three flow rates are shown by the graphs in Figures 8 and 9.

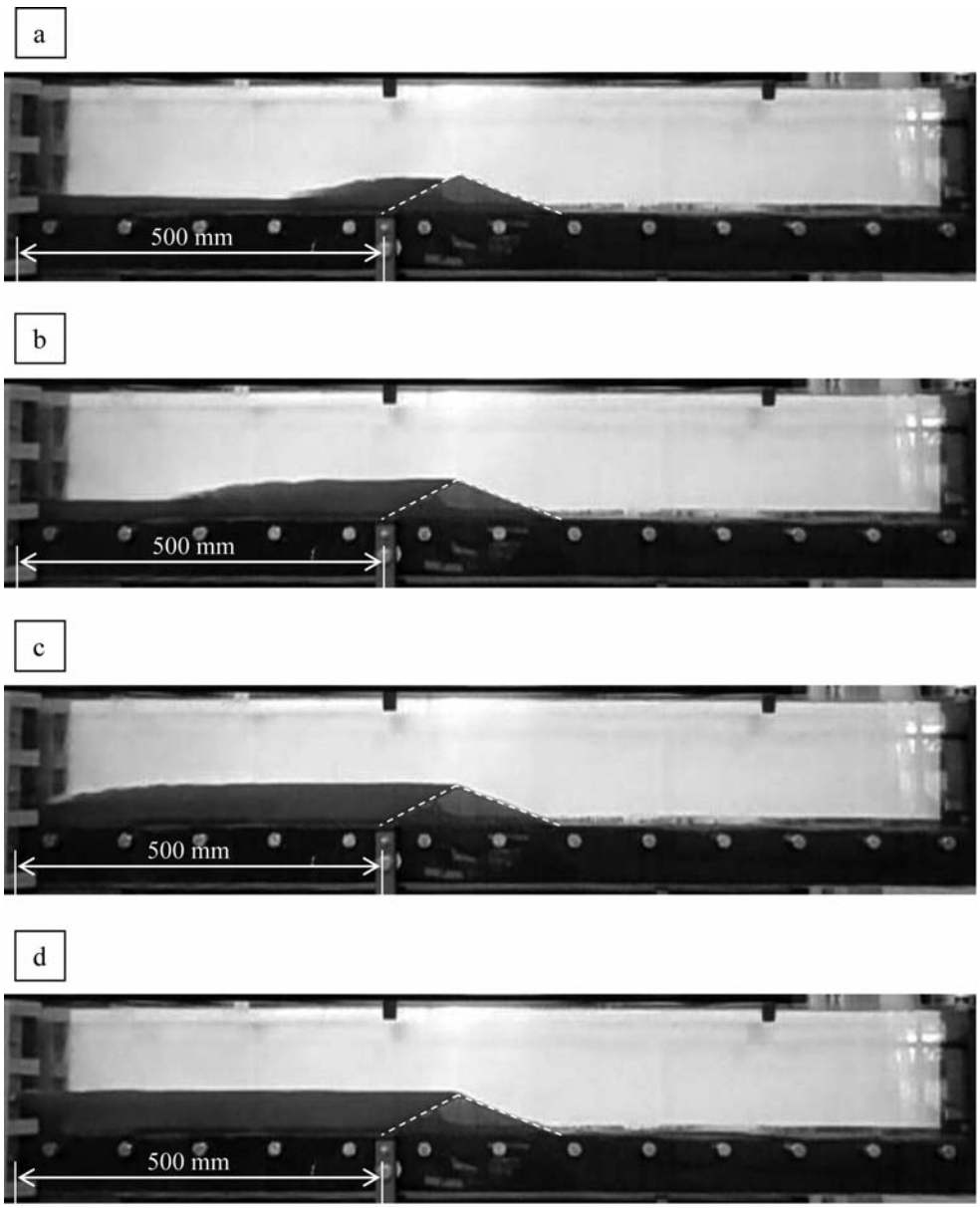

Figure 5 Sequential images of water flowing into the flume with a triangular weir (outlined with a dotted white line) at a flow rate of 3.0 $m^3.hr^{-1}$ at time: (a) t = 4.0 s; (b) t = 4.5 s; (c) t = 5.0 s; (d) t = 5.5 s.

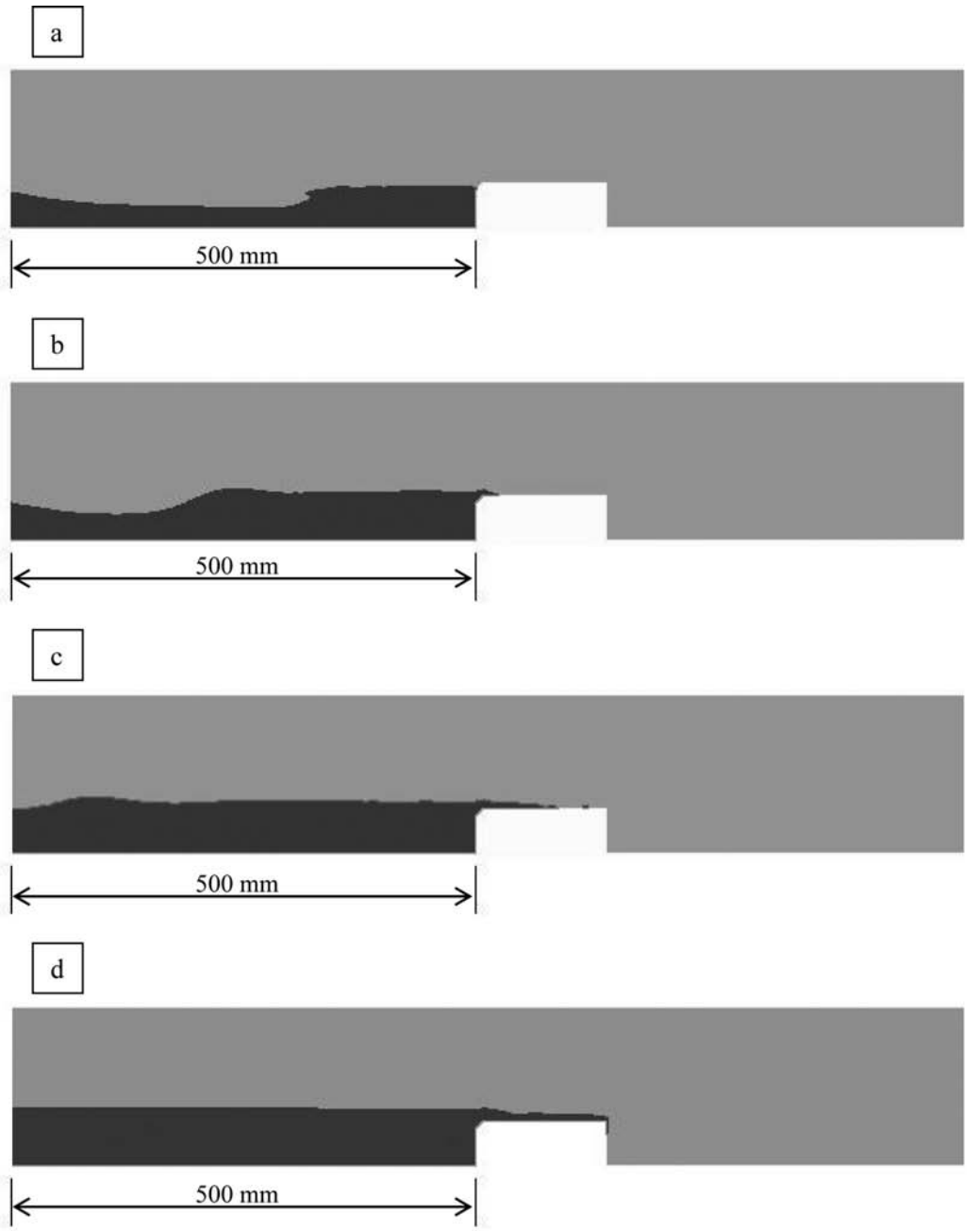

Figure 6 Compotational fluid dynamic results of water flowing into the flume with a rectangular weir (shown in white) at a flow rate of 3.0 $m^3.hr^{-1}$ at time: (a) t = 4.0 s; (b) t = 4.5 s; (c) t = 5.0 s; (d) t = 5.5 s.

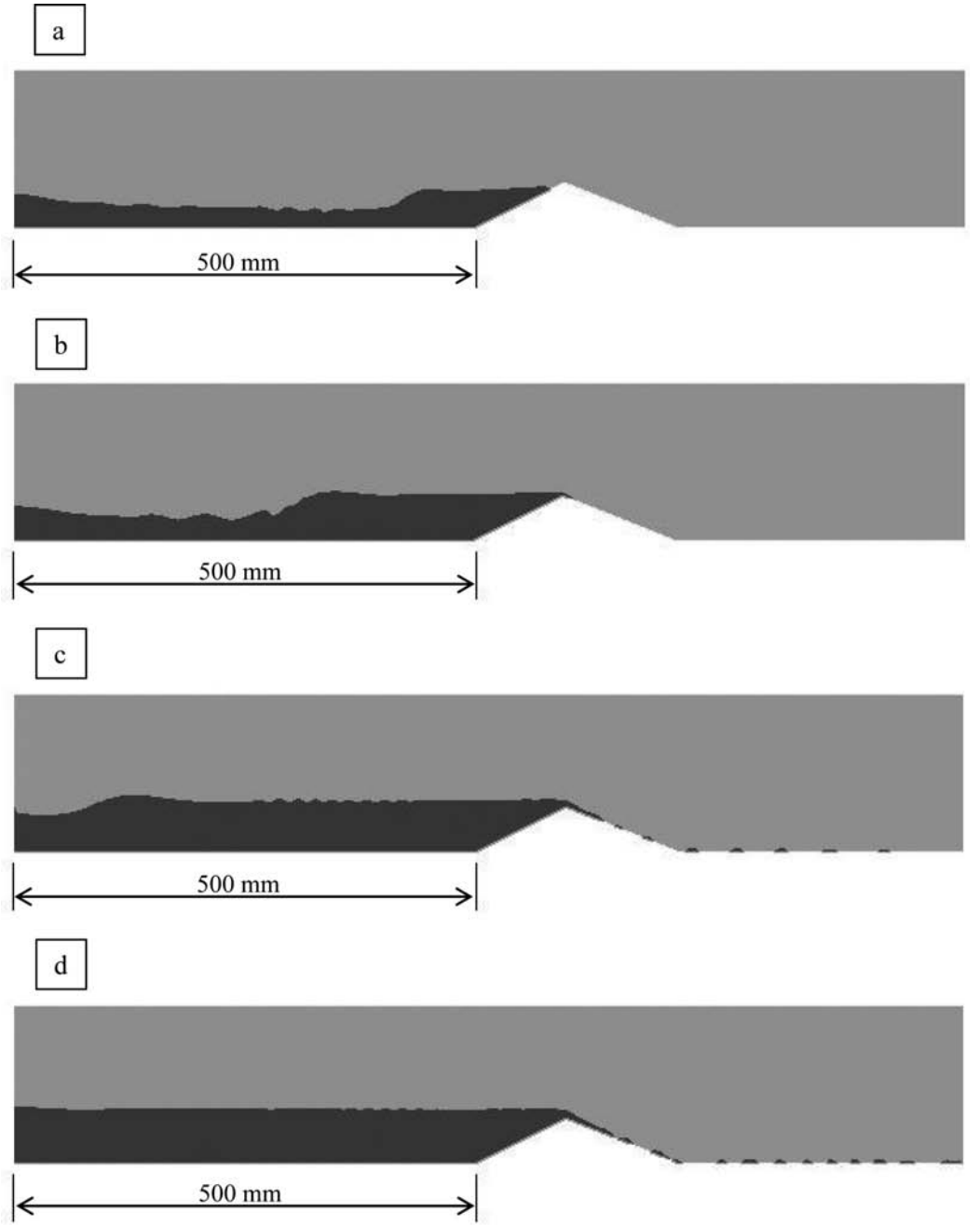

Figure 7 Computational fluid dynamic results of the water flowed into the flume with a triangular weir (shown in white) at flow rate of 3.0 $m^3.hr^{-1}$ at time: (a) t = 4.0 s; (b) t = 4.5 s; (c) t = 5.0 s; (d) t = 5.5 s.

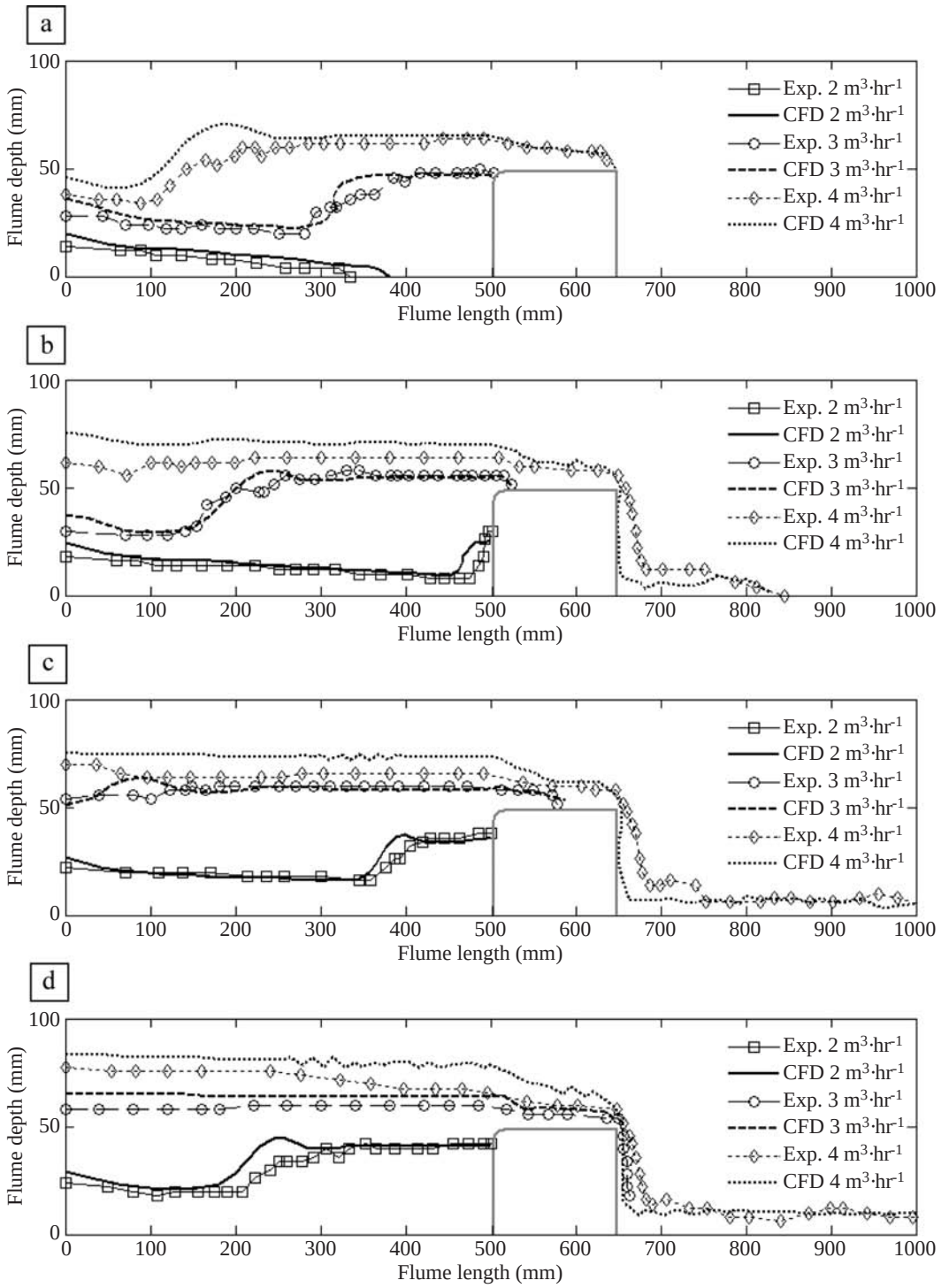

Figure 8 Surface profiles of water flowing into a flume with a rectangular weir at three flow rates (2.0, 3.0 and 4.0 $m^3.hr^{-1}$) for the experiment (Exp.) and the computational fluid dynamics (CFD) calculations in transient time periods of: (a) t = 4.0 s; (b) t = 4.5 s; (c) t = 5.0 s; (d) t = 5.5 s.

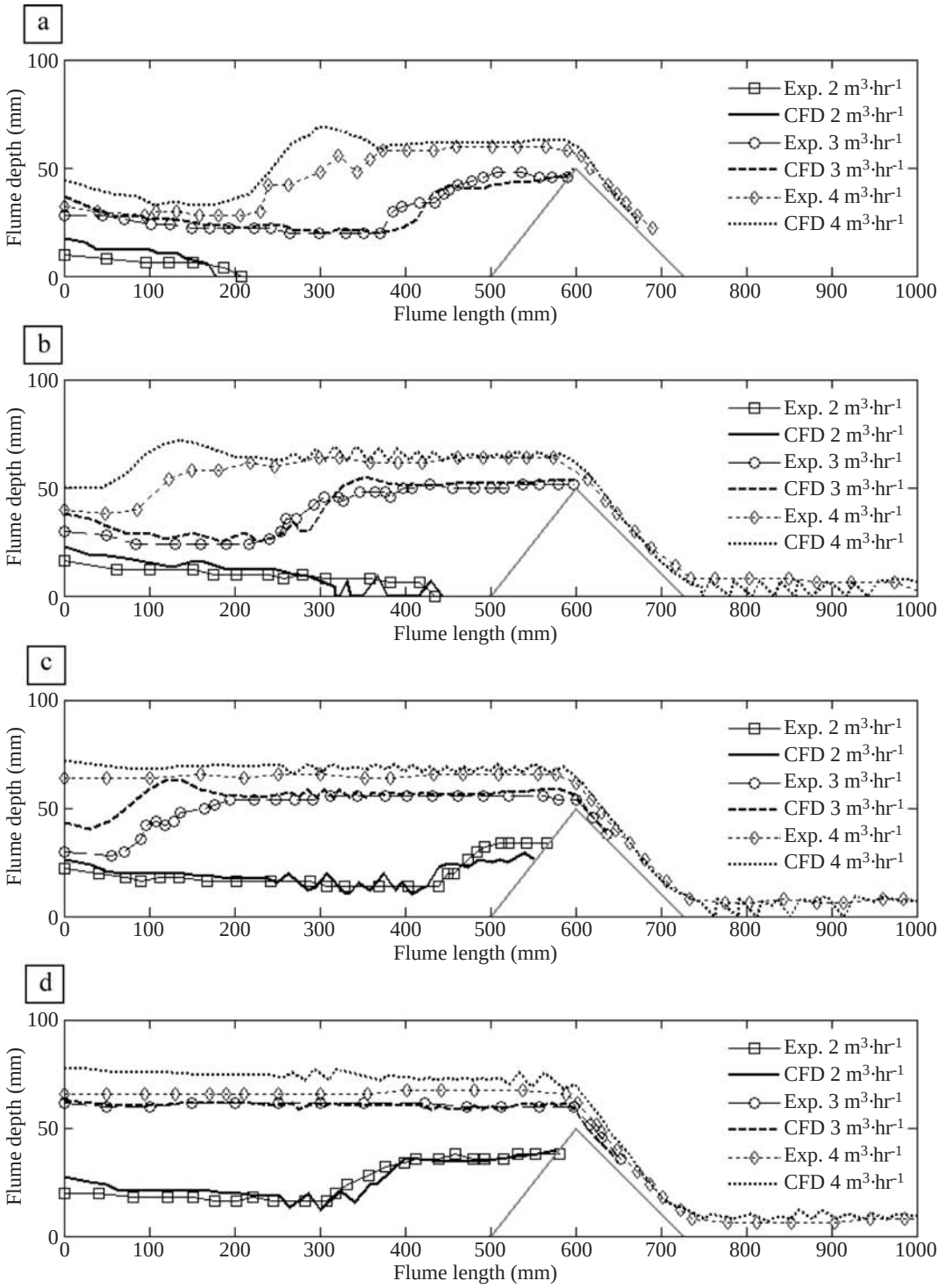

Figure 9 Surface profiles of water flowing into a flume with a rectangular weir at three flow rates (2.0, 3.0 and 4.0 $m^3.hr^{-1}$) for the experiment (Exp.) and the computational fluid dynamics (CFD) calculations in transient time periods of (a) t = 4.0 s; (b) t = 4.5 s; (c) t = 5.0 s; (d) t = 5.5 s.

It was observed that the crest of the water wave and the reversing wave moving upstream in the simulations both agreed with the experimental data. After water had overflowed the weirs ($t > 5.5$ s), the comparisons of the water profiles in steady time state are shown by the graphs in Figures 10 and 11 for the rectangular and triangular weir, respectively. The upstream water elevations corresponded between the CFD models and experiments for each flow rate. The surface profiles over the rectangular and triangular weirs, which are both broad-crested weirs, calculated by the CFD agreed with the experiments. Consequently, the flow velocity could be determined by the CFD models. The determination of the CFD errors was performed by splitting the time into transient and steady time periods. The transient time period was defined from when the water was distributed into the flumes until the weirs started to overflow. Subsequently, the steady time period was defined as the period from when the water overflowed the weirs and the surface profile did not change with time. The surface profiles of the CFD models had an average error compared with the experimental surface profiles as shown in Table 4.

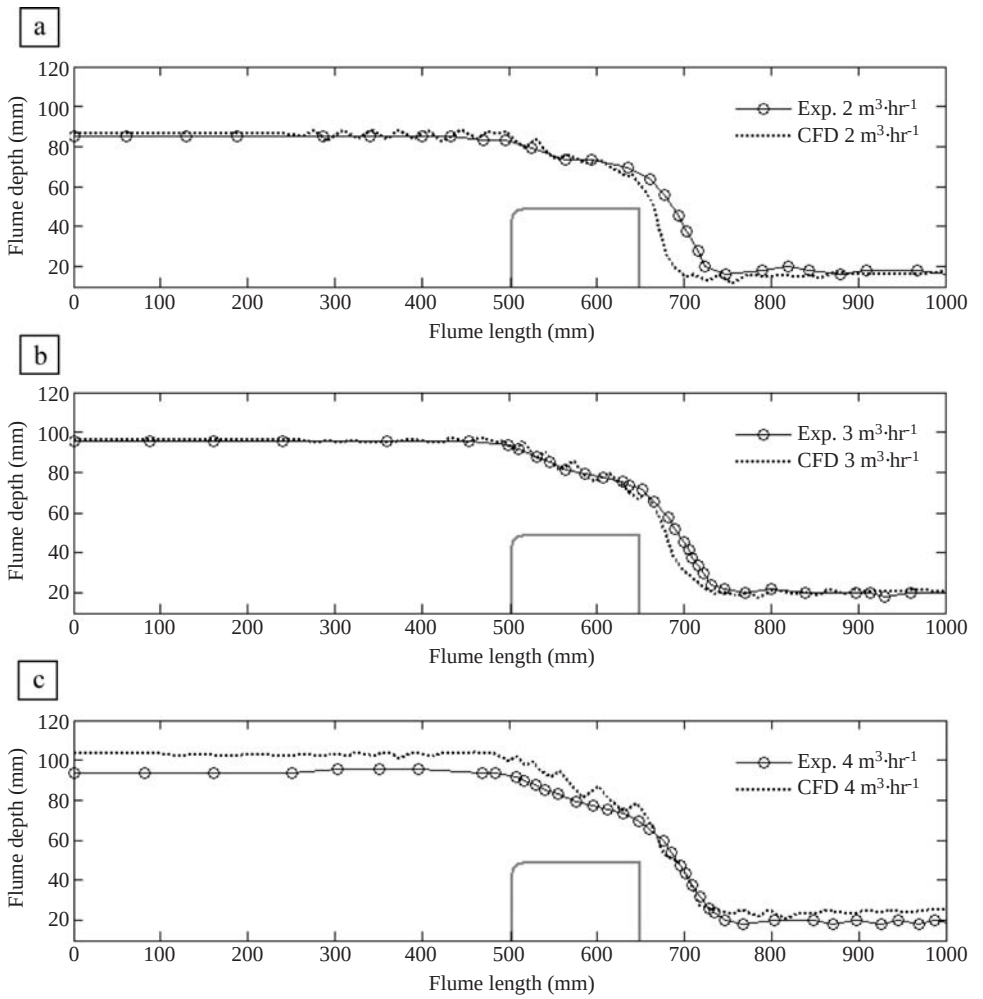

Figure 10 Surface profiles in the steady time period of water flowing into a flume with a rectangular weir for the experiment (Exp.) and the computational fluid dynamics (CFD) calculations at flow rates of: (a) 2.0 $m^3.hr^{-1}$; (b) 3.0 $m^3.hr^{-1}$; (c) 4.0 $m^3.hr^{-1}$.

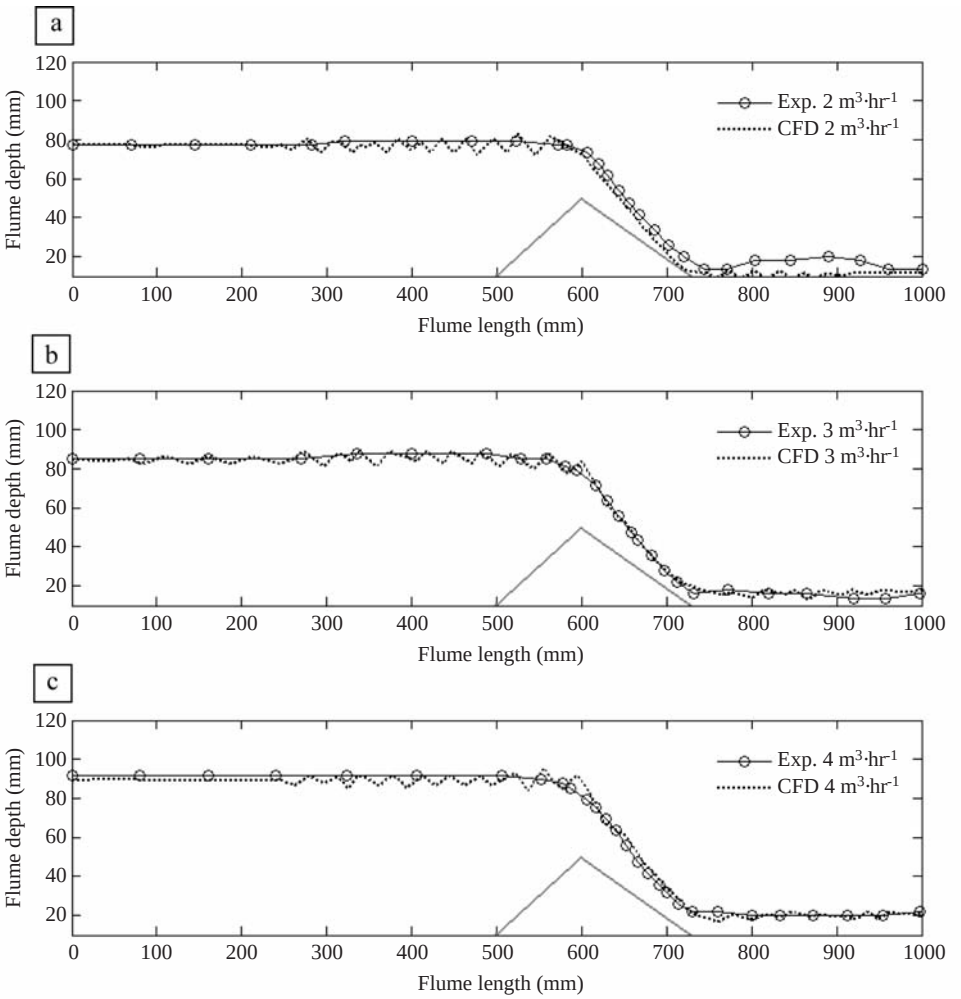

Figure 11 Surface profiles in the steady time period of water flowing into a flume with a triangular weir for the experiment (Exp.) and the computational fluid dynamics (CFD) calculations at flow rates of: (a) 2.0 $m^3.hr^{-1}$; (b) 3.0 $m^3.hr^{-1}$; (c) 4.0 $m^3.hr^{-1}$.

Table 4 Average error of the computational fluid dynamic (CFD) surface profiles compared with experiments at three flow rates.

CFD case	Weir type	Average error of CFD surface profiles compared with experiment (%)		
		Flow rate 2.0 $m^3.hr^{-1}$	Flow rate 3.0 $m^3.hr^{-1}$	Flow rate 4.0 $m^3.hr^{-1}$
Transient time	Rectangular	23.56	4.23	7.97
	Triangular	21.54	5.29	9.91
Steady time	Rectangular	7.07	2.06	15.14
	Triangular	13.16	4.81	0.98

CONCLUSION

The finite volume method (FVM) was applied to simulate the two phases of the turbulence flow based on the k-ε turbulence model. The developed code using the C++ language in open source software OpenFOAM was used for the simulation. The surface of water was defined using the Volume of Fluid (VOF) method. The water surface calculated using CFD was validated by setting up the experiments and digitized water surface images by the SloshDetector software. The profiles of the CFD surface in the transient time period and the steady time period had overall average errors of 8.94% and 8.06% when compared with the experimental surface profiles. The friction on the walls of the flume and the surface tension of the water had an impact on the accuracy of the CFD results, resulting in the surface heights of the water in the experiments being lower than in the CFD results.

The k-ε turbulence model was implemented and was found to be suitable for the two-phase flow equations in the simulation of the fluid flow in an open channel such as in a flume. The depths of the upstream flow were predicted by the developed codes, which agreed with the experiments. Furthermore, the combination of the turbulence and the free surface models was capable of explaining the complicated behavior of the fluid flow in the flumes that was associated with the surface jump or the wave crest in front of the weirs, the critical surface on broad-crested weirs and the supercritical surface profile downstream.

The case studies in this research validated and verified the codes developed using the OpenFOAM software. Therefore, the codes can be used for the design of novel weirs, and the codes can be expected to provide accurate measurement and appropriate flow structures. This adaptation will be further developed by compiling these codes into an executable file.

LITERATURE CITED

Cengel, Y.A. and J.M. Cimbala. 2010. **Fluid Mechanics: Fundamentals and Applications**, McGraw-Hill Company Inc. Singapore. 980 pp.

Chaichanasiri, E. and C. Suvanjumrat. 2012. Simulation of three dimensional liquid-sloshing models using C++ open source code CFD software. **Kasetsart J. (Nat. Sci.)** 46(6): 978–995.

French, R.H. 1987. **Open-Channel Hydraulics.** McGraw-Hill Company Inc. Singapore. 705 pp.

Hargreaves, D.M., H.P. Morvan and N.G. Wright. 2007. Validation of the volume of fluid method for free surface calculation: The broad-crested weir. **Eng. Appl. Comp. Fluid** 1(2): 136–146.

Haun, S., N.R.B. Olsen and R. Feurich. 2011. Numerical modeling of flow over trapezoidal broad-crested weir. **Eng. Appl. Comp. Fluid** 5(3): 397–405.

Henderson, F.M. 1966. **Open Channel Flow.** Macmillan Publishing Co. Inc. New York, NY, USA. 522 pp.

Issa, R.I. 1986. Solution of the implicitly discretised fluid flow equations by operator-splitting. **J. Comput. Phys.** 62: 40–65.

Launder, B.E. and D.B. Spalding. 1974. The numerical computation to turbulent flows. **Compt. Method. Appl. M.** 3(2): 269–289.

Munson, B.R., D.F. Young, T.H. Okiishi and W.W. Huebsch. 2010. **Fundamentals of Fluid Mechanics.** John Wiley & Sons Inc. Singapore.723 pp.

OpenFOAM. 2009. **Programmer's Guide.** OpenCFD Limited. Boston, MA, USA. 95 pp.

Saker, M.A. and D.G. Rhodes. 2004. Calculation of free-surface profile over a rectangular broad-crested weir. **Flow Meas. Instrum.** 15: 215–219.

Suvanjumrat, C. and T. Puttapitukporn. 2010. Sloshing surface monitoring using image processing. *In* **The First TSME International Conference on Mechanical Engineering**. 20-22 October 2010, Ubon Ratchathani, Thailand. 110 pp.

Versteeg, H.K. and W. Malalasekera. 2007. **An Introduction to Computational Fluid Dynamics; The Finite Volume Method.** Prentice Hall. Essex, UK. 503 pp.

Yeoh, G.H. and J. Tu. 2010. **Computational Techniques for Multi-phase Flows.** Butterworth-Heinemann publications. MA, USA. 643 pp.

Yeung, H. 2007. An examination of BS3680 4C (ISO/DIS 4369) on the measurement of liquid flow in open channels – flumes. **Flow Meas. Instrum.** 18: 175–182.